

Supporting Information for

Observation of High Seebeck Coefficient and Low Thermal Conductivity in New [SrO]-intercalated CuSbSe₂ Compound

Kejun Bu,^{†, ‡} Jian Huang,[†] Mengjia Luo,^{†, ‡} Mengjia Guan,^{†, ‡} Chong Zheng,[#] Jie Pan,[†] Xian Zhang,[§] Sishun Wang,[†] Wei Zhao,[†] Xun Shi,[†] Li Xu,[‡] and Fuqiang Huang^{*, †, §}

[†]State Key Laboratory of High Performance Ceramics and Superfine Microstructure, Shanghai Institute of Ceramics, Chinese Academy of Sciences, Shanghai 200050, P. R. China

[‡]University of Chinese Academy of Sciences, Beijing 100049, China

[§]State Key Laboratory of Rare Earth Materials Chemistry and Applications, College of Chemistry and Molecular Engineering, Peking University, Beijing 100871, P.R. China

[#]Department of Chemistry and Biochemistry, Northern Illinois University, DeKalb, Illinois 60115, United States

[‡]Material Laboratory of State Grid Corporation of China, State Key laboratory of Advanced Transmission Technology, Global Energy Interconnection Research Institute Co., Ltd., Beijing 102209, China

List of contents:

- 1. Experimental section.**
- 2. Crystal structure details.**
- 3. Transmission electron microscopy details.**
- 4. Electron localization function details.**
- 5. Supplementary equations.**
- 6. Supplementary figures.**
- 7. Supplementary tables.**

1. Experimental Section

Reagents. All starting materials were obtained from Alfa Aesar without further purification: (i) SrSe, 99%; (ii) CuO, 99.9%; (iii) Antimony powder, 99.9%; (iv) Selenium powder, 99.9%; (v) CsI, 99.9%. All reagents were kept in an Ar-protected glove box prior to use.

Synthesis of SrOCuSbSe₂ Single Crystals. Single crystals of SrOCuSbSe₂ were synthesized by traditional melting salt method. A mixture of starting materials of 1 mmol of SrSe, 1 mmol of CuO, 1 mmol of Sb powder, 1 mmol of Se powder, and 50 mmol of CsI powder was loaded in a carbon-coated fused silica tube. The tube was flame-sealed under vacuum ($< 10^{-3}$ mbar) and heated slowly to 1073 K with a programmable furnace. Afterward, the silica tube was kept at this temperature for 2 days followed by cooling to 773 K at a rate of 2K/h and finally quenched in air. The melts were taken out and transferred into 150 mL of deionized water, followed by ultrasonic washing several times and drying by ethanol. Finally, a great number of black rod-shaped crystals were obtained. The presence of Sr, Cu, Sb, Se, and O was confirmed by semi-quantitative energy-dispersive X-ray (EDX) analysis on a JEOL (JSM6510) scanning electron microscope.

Synthesis of SrOCuSbSe₂ Powder. Powder of SrOCuSbSe₂ was synthesized by solid-state reaction of stoichiometric amount of SrSe, CuO, Sb powders and Se powders in a sealed fused-silica tube evacuated to 10^{-3} mbar. The samples were slowly heated to 873 K at $2\text{ K}\cdot\text{min}^{-1}$, held for 2 days, and the furnace cooled to room temperature. The harvested powder was ground, sealed, and calcined for 2 days at the same temperature. The final powder was densified in a spark plasma sintering (SPS) furnace in a graphite die (Φ 10mm) under a pressure of 60 MPa at 823 K, held for 5 min in argon atmosphere. The obtained pellets had relative densities larger than 95% of the theoretical value (5.857 g/cm^3).

Single Crystal X-ray Crystallography. Suitable crystal was chosen to perform the data collections. Single crystal X-ray diffraction was performed on a Bruker D8QUEST diffractometer equipped with Mo $K\alpha$ radiation. The diffraction data were collected at room temperature by the ω - and φ - scan methods.¹ The crystal structure was solved and

refined using the APEX3 program. Absorption corrections were performed using the multi-scan method (SADABS). The detailed crystal data and structure refinement parameters are summarized in Table S4. Fractional atomic coordinates parameters, atomic displacement parameters, selected bond distances and bond angles are summarized in Table S5-S7 in Supporting Information.

Powder X-ray Diffraction. The as-synthesized crystal samples were ground into fine powder before use. Phase purity of the powder samples was checked by powder X-ray diffraction performed on a Bruker D8QUEST diffractometer equipped with mirror-monochromatized source of Cu $K\alpha$ radiation ($\lambda = 0.15406$ nm). The patterns were recorded in a slow-scanning mode with 2θ from 5° to 80° at a scan rate of $2^\circ/\text{min}$. Simulated patterns were generated by using the CrystalMaker program and CIF file of the refined single crystal structure.

Electron microscopy. Transmission electron microscopy (TEM) investigations were performed using a JEOL GRAND ARM (JEOL, Tokyo, Japan) microscope operating at 300 kV. The TEM specimens were prepared by focused ion beam (FIB, Helios nanolab 600, FEI, USA). The procedures were performed including the cutting, grinding, dimpling, polishing and Ar-ion milling in a liquid nitrogen environment.

Solid-state UV-Vis Spectroscopy. The solid-state ultraviolet-visible (UV-Vis) light diffuse-reflectance spectra of the fine powder of SrOCuSbSe_2 was measured on a UV-4100 spectrophotometer operating from 1200 to 350 nm at room temperature. BaSO_4 powder was used as a 100% reflectance standard. The powder sample was spread on a compacted base of BaSO_4 powder. The generated reflectance-versus-wavelength data were used to measure the band gap of the as-synthesized samples. The reflectance data were converted to absorbance data by using the Kubelka-Munk equation.²

Thermal Analyses. Thermogravimetric analysis (TG) and differential thermal analysis (DTA) were carried out on a NETZSCH STA449C thermal analyzer for investigating the thermal properties of the SrOCuSbSe_2 compound. A well-ground powder sample (9.46 mg) was loaded into an Al_2O_3 crucible and heated from room temperature to 900°C at $10^\circ\text{C}/\text{min}$ under a constant flow of argon gas.

Transport Property Measurement. The high temperature (300–850 K) electrical resistivity (ρ) and Seebeck coefficient (S) were simultaneously measured using an ULVAC-RIKO ZEM 3 apparatus. For this measurement, bar samples about 1.5 mm×2 mm×10 mm were used. Electrical conductivity was measured by a four-probe method. Thermoelectromotive force (ΔE) at the test temperature was measured using five different temperature gradients ($0 < \Delta T < 2$ K) to calculate the Seebeck coefficient from the ΔE versus ΔT plot. Thermal diffusivity coefficient λ was determined using a laser-flash method in a flowing Ar atmosphere (Netzsch LFA 427) (Figure S13). The thermal conductivity was calculated from $k = C_p \rho \lambda$, where ρ is the density and C_p is the specific heat capacity. The C_p is estimated using the Dulong-Petit model ($C_p = 3k_b/\text{atom}$), which matches well with the experimental results (Figure S12). The Wiedemann-Franz law, using a Lorentz number of $1.5 \times 10^{-8} \text{ W} \cdot \Omega \cdot \text{K}^{-2}$, was used to calculate the lattice thermal conductivity by subtracting the electronic contribution from the total thermal conductivity ($k_L = k - k_e$). Low-temperature electrical resistivity (2–300 K), room-temperature Hall effect measurements (-2 T–2 T) and specific heat capacity were measured using a Physical Properties Measurements System (PPMS–Quantum Design Dyna Cool). The formula $p = 1/R_H e$, was used to calculate the carrier concentration by the approximation of single parabolic band conduction model.

Electronic Structure Calculation. First principles calculations were performed using the Vienna Ab Initio Simulation Package (VASP).³⁻⁵ The Perdew-Burke-Ernzerhof (PBE) version of the generalized gradient approximation (GGA) was used to describe the exchange correlation functional, and the projector augmented wave (PAW) method was used in the present work.⁶ Here the cutoff energy of plane wave was chosen at 480 eV. For the structure optimizations, $6 \times 10 \times 5$ k-points were used for the conventional cell. The convergence criteria were that the change in total energies between two successive electronic steps was less than 10^{-5} eV, and all the Hellmann-Feynman force acting on each atom was less than 0.01 eV /Å. High-symmetry points in Brillouin zones (X, Γ , Z, B, and A represent (0.5, 0.5, 0), (0, 0, 0), (0, 0.5, 0), (0, 0, 0.5), and (-0.5, 0, 0.5)) were considered in our band structure calculation.

Phonon calculations. To study the lattice dynamics of SrOCuSbSe₂, Phonopy as interfaced with VASP was used to calculate the phonon properties based on finite displacement methods.⁷⁻⁸ A supercell with dimensions of 2×4×2 (including 192 atoms) was constructed. High-symmetry points in the Brillouin zone (X, Γ , Y, S, R, T, and Z represent (0.5, 0, 0), (0, 0, 0), (0, 0.5, 0), (0.5, 0.5, 0), (0.5, 0.5, 0.5), (0, 0.5, 0.5), and (0, 0, 0.5)) were considered in our phonon dispersion and Grüneisen parameter calculations.

2. Crystal structure details

As shown in Figure S1a, the SrOCuSbSe₂ structure can be regarded as the combination of the insulating SrO and distorted conductive CuSbSe₂ structural units. The SrO layer intercalated into interlayers of the original structure CuSbSe₂ (D_{2h}^{16} - $Pnma$) leads to distorted CuSbSe₂ layers, and results in the lower symmetry SrOCuSbSe₂ structure. The SrOCuSbSe₂ compound crystallizes in the C_{2h}^2 - $P2_1/m$ (No. 11) space group of the monoclinic system (Table S4). The structure consists of one independent Sr site (2e), one independent Cu site (2e), one independent Sb site (2e), one independent O site (2e), and two independent Se sites (2e) (Table S5). The structure features quasi-2D ${}^2_{\infty}[\text{CuSbSe}_2\text{O}]^{2-}$ anionic layers, which are separated by Sr²⁺ ions (Figure S1a-b). Each ${}^2_{\infty}[\text{CuSbSe}_2\text{O}]^{2-}$ anionic layer is composed of infinite ${}^1_{\infty}[\text{CuSe}_4]^{7-}$ chain interconnected by square-pyramidal $[\text{SbSe}_4\text{O}]^{7-}$ primary building units via one edge sharing and two vertices sharing (Figure S1b-e). The distorted $[\text{CuSe}_4]^{7-}$ tetrahedra are aligning along the *b* axis via edge sharing, and in turn form the ${}^1_{\infty}[\text{CuSe}_4]^{7-}$ chains (Figure S1c). As shown in Figure S1d-e, the Sb³⁺ ions center the severely distorted square pyramids formed by basal two Se(1) atoms and two Se(2) atoms, and one apical O atom. The edge sharing $[\text{SbSe}_4\text{O}]^{7-}$ square pyramids also form continuous chains along the *b* axis and connect two ${}^1_{\infty}[\text{CuSe}_4]^{7-}$ chains.

The distances between Cu and Se range from 2.47 to 2.52 Å, and the Se–Cu–Se angles are between 111.65 and 112.59° (Figure S1f), comparable to the Cu–Se distances in the reported structures (2.43 Å in CuSbSe₂,⁹ 2.52 Å in BaCuSbSe₃,¹⁰ and 2.50 Å in

Cu_3SbSe_3).¹¹ The intrachain Cu–Cu distances are 2.79 Å, suggesting weak d^{10} – d^{10} interaction (less than 2.8 Å).¹² The distance of the Sb–Se(2) bond is 2.78 Å, while distance of the Sb–O bond is 1.94 Å (Figure S1f). The $5s^2$ lone pair of Sb^{3+} points toward Se(1) with an Sb–Se(1) distance of 3.04 Å. This long distance implies a relatively weak interaction. The Se(2)–Sb–Se(2) and Se(2)–Sb–O angles are 92.59 and 90.88°, respectively. In the Cu–Sb–Se system, the average Se–Sb–Se bond angles are 109.5° in Cu_3SbSe_4 ,¹³ 95.24° in CuSbSe_2 ,⁹ and 99.42° in Cu_3SbSe_3 .¹¹ The reason for the large thermal conductivity difference between Cu_3SbSe_4 , CuSbSe_2 , and Cu_3SbSe_3 is the electrostatic repulsion between the $5s^2$ lone pair electrons on the Sb atoms and neighboring Se ions. This repulsive force changes the Se–Sb–Se bond angles and results in strong vibrational anharmonicity in the lattice.^{14–15} Therefore, it is reasonable to assume that SrOCuSbSe_2 would have an ultralow thermal conductivity. Sr has 8-fold coordination with five Se atoms and three O atoms to form an irregular coordinated polyhedron with distances of the Sr–Se and Sr–O bonding varying from 3.23 to 3.36 Å and from 2.50 to 2.56 Å, respectively (Figure S1f).

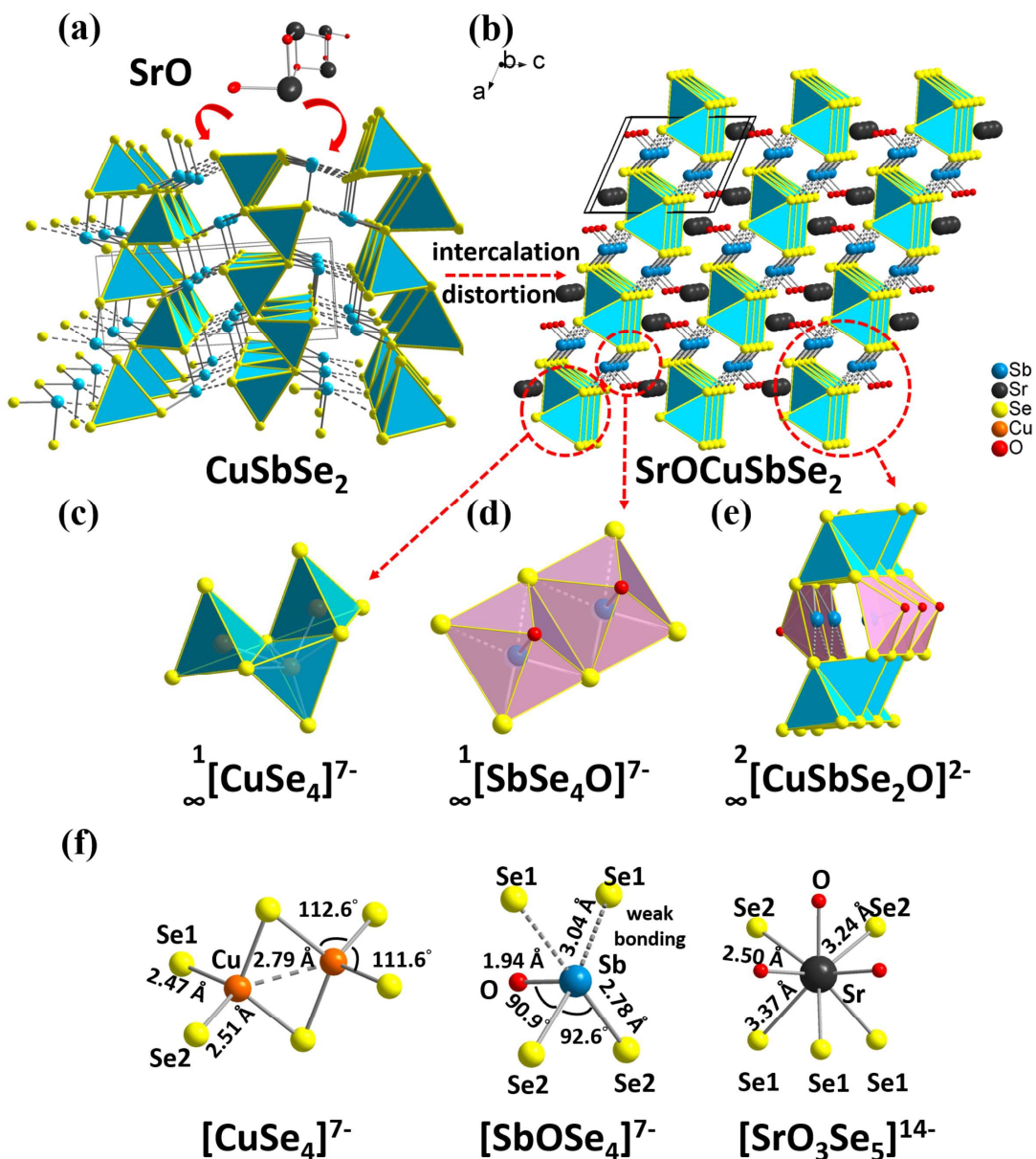


Figure S1. (a) Schematic diagram of the transformation from the CuSbSe_2 to SrOCuSbSe_2 . (b) 2D ${}^2_{\infty}[\text{CuSbSe}_2\text{O}]^{2-}$ layers of SrOCuSbSe_2 along the b direction, the Sr^{2+} cations are located between the layers. Black atoms: Sr; yellow atoms: Se; blue tetrahedra: CuSe_4 ; pink square pyramids: SbSe_4O . The building blocks: (c) Infinite ${}^1_{\infty}[\text{CuSe}_4]^{7-}$ chains. (d) Square-pyramidal ${}^1_{\infty}[\text{SbSe}_4\text{O}]^{7-}$ units. (e) 2D ${}^2_{\infty}[\text{CuSbSe}_2\text{O}]^{2-}$ layers; the SbSe_4O units connects two ${}^1_{\infty}[\text{CuSe}_4]^{7-}$ chains on opposite directions. (f) Coordination the polyhedra of the cations in SrOCuSbSe_2 .

3. Transmission electron microscopy details

The compound SrOCuSbSe_2 was examined in more details using TEM. Figure S2a shows the low-magnification TEM image of FIB SrOCuSbSe_2 sample. The FIB sample with an average width of 3 μm and length of 3 μm is shown in the image. The electron diffraction pattern can be easily indexed as the $[-1\ 0\ 0]$ direction of the SrOCuSbSe_2 sample (Figure S2b inset). The relative electron diffraction pattern shows no split spots along the $[-1\ 0\ 0]$ axis, instead revealing two sublattices (CuSbSe_2 and SrO) that are commensurate rather than incommensurate. These data suggest that SrOCuSbSe_2 is not a misfit compound. The distance of the layer along the c axis is about 0.86 nm in the high-resolution TEM image (Figure S2b), which is consistent with distances of crystal structure information (Figure S2d). Figure S2c is the atomic model based on the spherical aberration corrected TEM, which clearly presents separation between SrO layers and CuSbSe_2 layers along the $[-1\ 0\ 0]$ direction and matches well with the crystal structure image (Figure S2c and Figure S2d).

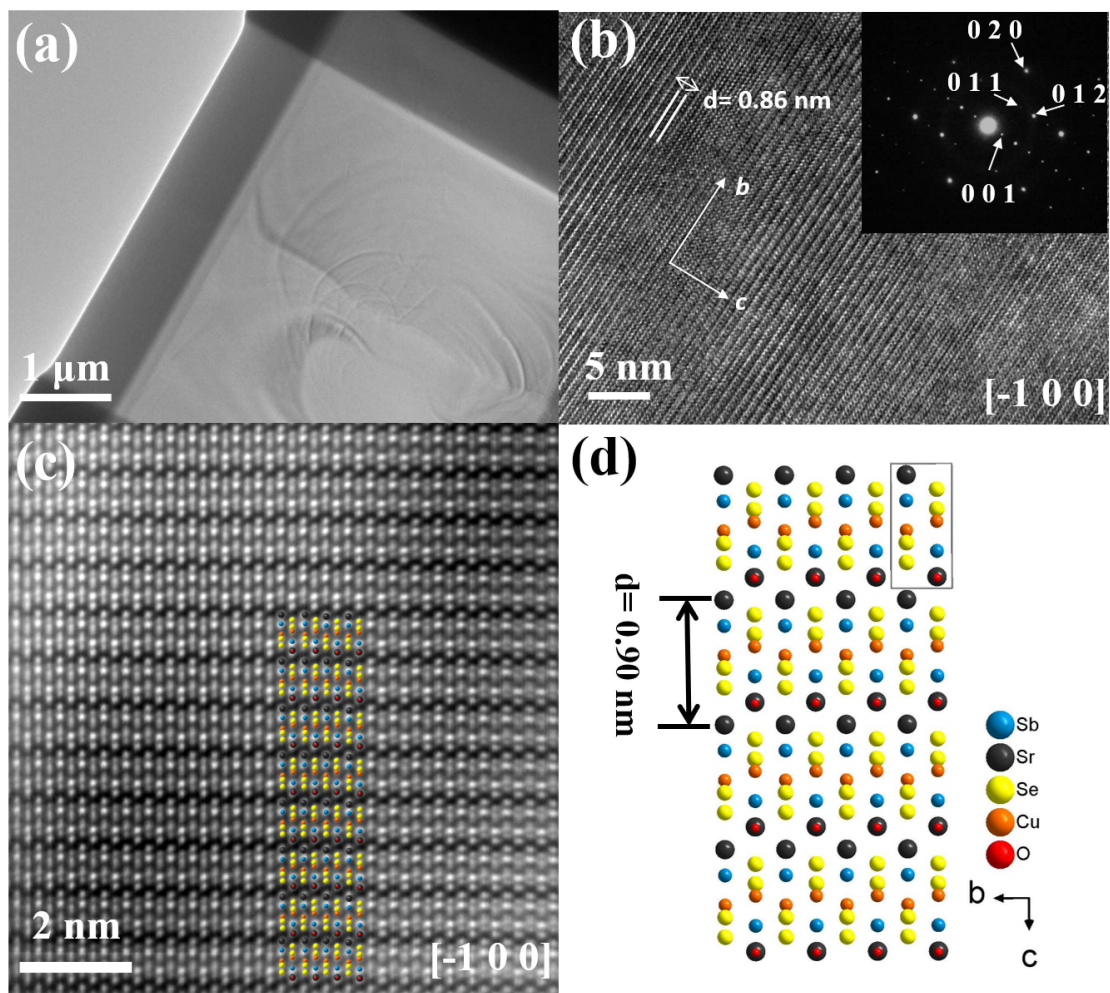


Figure S2. (a) Low magnification TEM image of the FIB SrOCuSbSe₂ sample. (b) High-resolution TEM image of the SrOCuSbSe₂ sample. (inset) Select area electron diffraction from the FIB region. (c) The atomic model based on the spherical aberration corrected TEM. (d) The crystal structure of the SrOCuSbSe₂ along the $[-1\ 0\ 0]$ direction.

4. Electron localization function details

The bonding nature of SrOCuSbSe₂ was also analyzed through the calculated electron localization function (ELF) (Figure S3a). The isosurface of the charge illustrates the lobe-like extension around the Sb atoms, indicating the classic signatures of $5s^2$ lone-pair

electrons. We speculate that the low thermal conductivity is related to the enhancement of the anharmonicity in the lattice, which is caused by the overlapping wave functions of the lone-pair electrons and nearby valence electrons that induce nonlinear repulsive electrostatic forces.¹⁴ Hence for SrOCuSbSe₂, the high degree of anharmonicity should be achieved when the lone-pair electron is far removed from the Sb nucleus and not participating in bonding, such as Sb–Se1 weak bonding, leading to the distorted coordination and making an ultra-low thermal conductivity.¹⁵ According to the X–Sb–X average bond angle ($\bar{\alpha}$), the effective valence of the Sb³⁺ in the SrOCuSbSe₂ can be derived to show how far the lone-pair electrons are removed from Sb atoms (Equation S1):¹⁴

$$^{\text{eff}}V_{\text{Sb}^{3+}}(\bar{\alpha}) = 3[1 + 0.0128(\bar{\alpha} - 90)] \quad (1)$$

The $^{\text{eff}}V_{\text{Sb}^{3+}} = 3.15$ for SrOCuSbSe₂, compared to $^{\text{eff}}V_{\text{Sb}^{3+}} = 3.20$ for CuSbSe₂ and 3.36 for Cu₃SbSe₃, indicating that lone-pair is farthest removed from the Sb nucleus in Cu₃SbSe₃. Therefore, it is reasonable that the thermal conductivity of SrOCuSbSe₂ is comparable to that of CuSbSe₂ and slightly higher than Cu₃SbSe₃ (Table S3). The charge projection on the (0 1 0) surface is shown in Figure S3b, the Sb–O and Sb–Se2 atoms are connected via covalent bonding, while the Cu atoms connect with neighboring Se1 and Se2 via ionic bonding. Notably, the Sb–Se1 atoms are connected via quite weak covalent bonding and show the overlap wave functions of the Sb 5s² lone-pair electrons and Se1 *p* electrons, which induce strong lattice anharmonicity and result in low thermal conductivity.

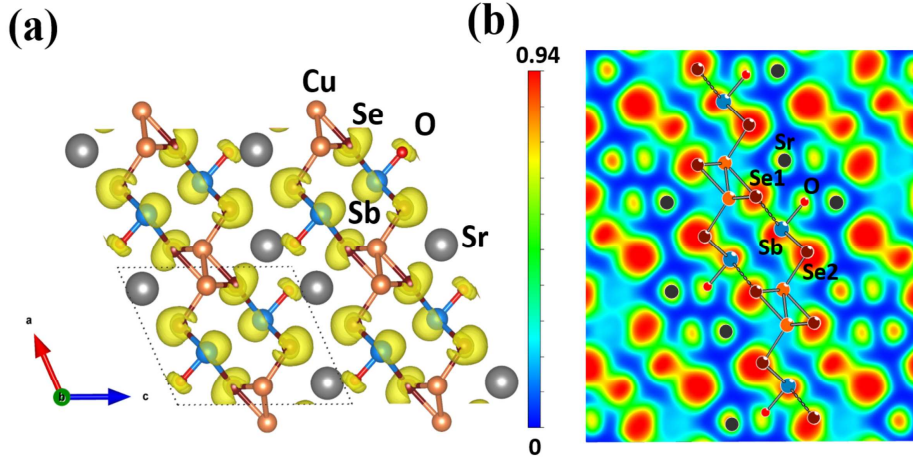


Figure S3. (a) The ELF graph of SrOCuSbSe_2 : ball-and-stick models with an isosurface value of 0.84. (b) Valence electron density map project onto the (0 1 0) plane showing the coordination of Sr, O, Cu, Sb, Se1 and Se2 atoms.

5. Supplementary equations

The small polaron hopping (SPH) model and variable range hopping (VRH) model are two well-known models that can be used to describe the semiconducting transport.¹⁶⁻¹⁷ The electrical resistivity due to polaron hopping conduction satisfies the Arrhenius like relation, namely:

$$\rho_T = \rho_0 \exp\left(\frac{E_p}{K_B T}\right) \quad (2)$$

Where E_p is the total activation energy of a polariton. The VRH model can be expressed as:

$$\rho_T = \rho_0 \exp\left(\frac{T_0}{T}\right)^{1/4} \quad (3)$$

Where $T_0 = \frac{\beta}{\kappa g(\mu) a^3}$, $g(\mu)$ is the density of states at the Fermi level, a is the localization radius of the states near the Fermi level, and β is a numerical coefficient.

The effective mass m^* is estimated according to the following equation using the observed carrier concentration (n_h) and Seebeck coefficient (S) values.¹⁸⁻¹⁹

$$m^* = \frac{h^2}{2k_B T} \left[\frac{n}{4\pi F_{1/2}(\eta)} \right]^{\frac{2}{3}} \quad (4)$$

$$S = \pm \frac{k_B}{e} \left(\frac{(r + 3/2)F_{r+3/2}(\eta)}{(r + 3/2)F_{r+1/2}(\eta)} - \eta \right) \quad (5)$$

$$F_n(\eta) = \int_0^\infty \frac{\chi^n}{1 + e^{\chi - \eta}} d\chi \quad (6)$$

Where η is the reduced Fermi energy, $F_n(\eta)$ is the n^{th} order Fermi integral, k_B is the Boltzmann constant, e is the electron charge, h is the Planck constant and r is the scattering factor. The scattering factor (r) is -1/2 as the acoustic phonon scattering is independent of the grain size and is generally assumed to be the main scattering mechanism at room temperature.

The lattice thermal conductivity (k_L) values were estimated by subtracting the carrier thermal conductivity (k_e) from the total k :

$$k_L = k - k_e \quad (7)$$

Where the Wiedemann-Franz relation with a Lorenz constant of $L_0 = 1.58 \times 10^{-8} \text{ V}^2 \cdot \text{K}^{-2}$ is applied for estimating k_e .²⁰

$$k_e = L_0 \sigma T \quad (8)$$

Because of the low k_L , it is worth comparing it with the calculated minimum lattice thermal conductivity k_{Lmin} for SrOCuSbSe_2 . The k_L value can be estimated by the following relationship:²¹⁻²²

$$k_L = \frac{1}{3} C_v v_a l \quad (9)$$

where the C_v is the molar specific heat at constant volume, l is the mean free path of phonons, and v_a is the average sound velocity, which is defined by the following relationship:²²⁻²³

$$v_a = \left(\frac{1}{3} \left[\frac{1}{v_l^3} + \frac{2}{v_s^3} \right] \right)^{-1/3} \quad (10)$$

where v_a is determined using the longitudinal (v_l) and transverse (v_s) sound velocities which are provided in Table S2. The minimal k_{Lmin} is estimated by the minimum l to be the interatomic distance of $\sim 3.0 \text{ \AA}$ for SrOCuSbSe_2 .

6. Supplementary figures

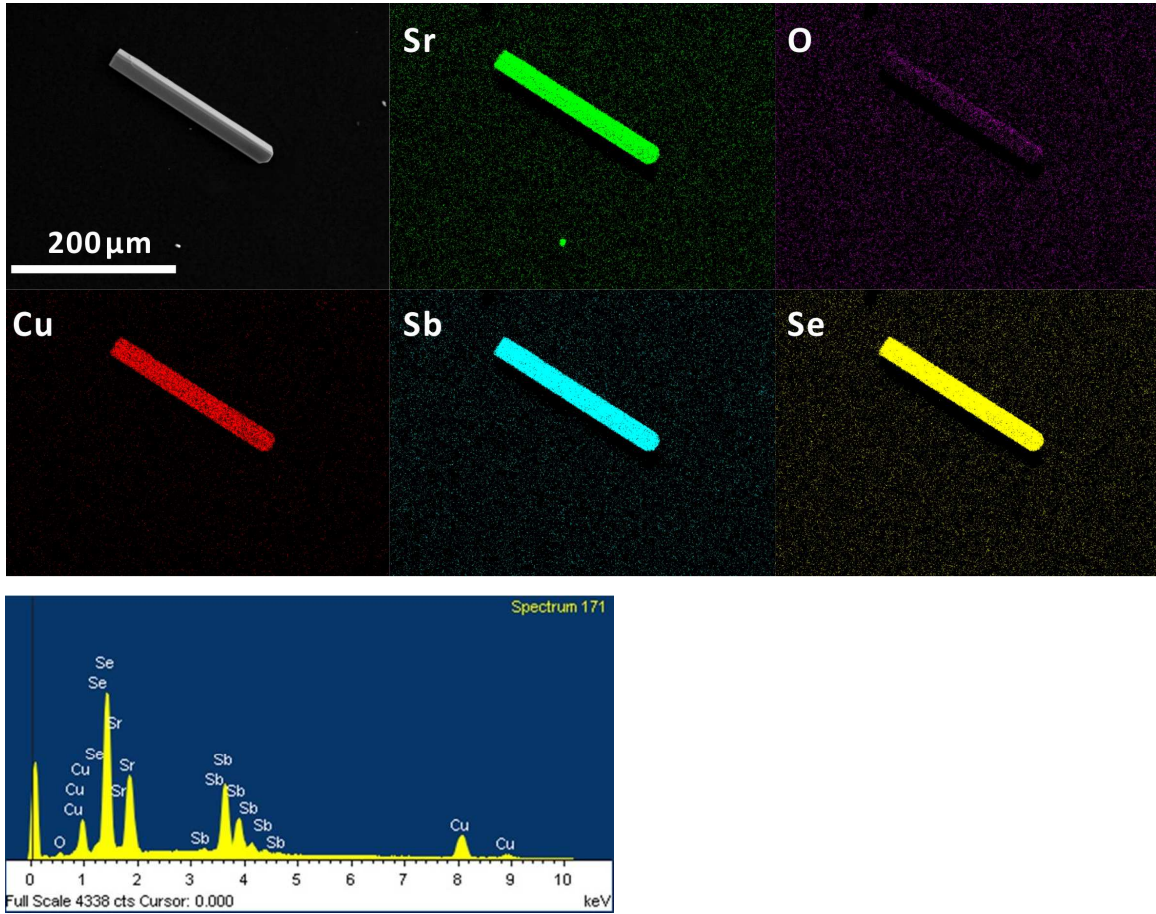


Figure S4. The SEM image and EDS result of SrOCuSbSe_2 crystal, and element mapping of Sr, O, Cu, Sb and Se in SrOCuSbSe_2 .

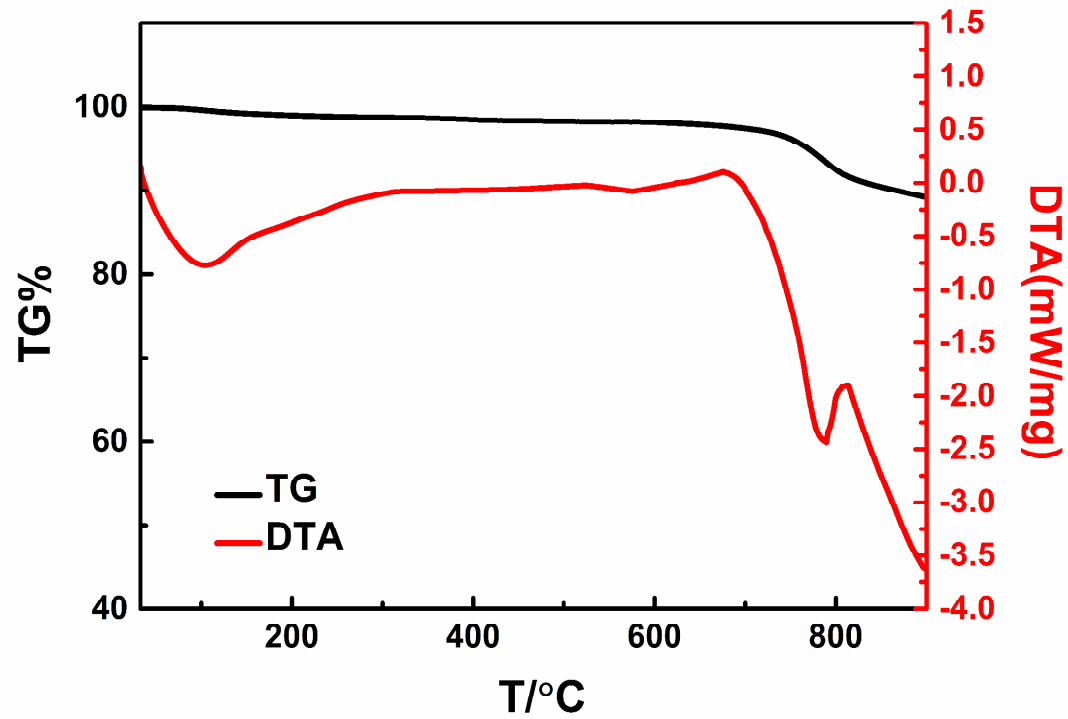


Figure S5. TG (black) and DTA (red) diagrams of SrOCuSbSe_2 .

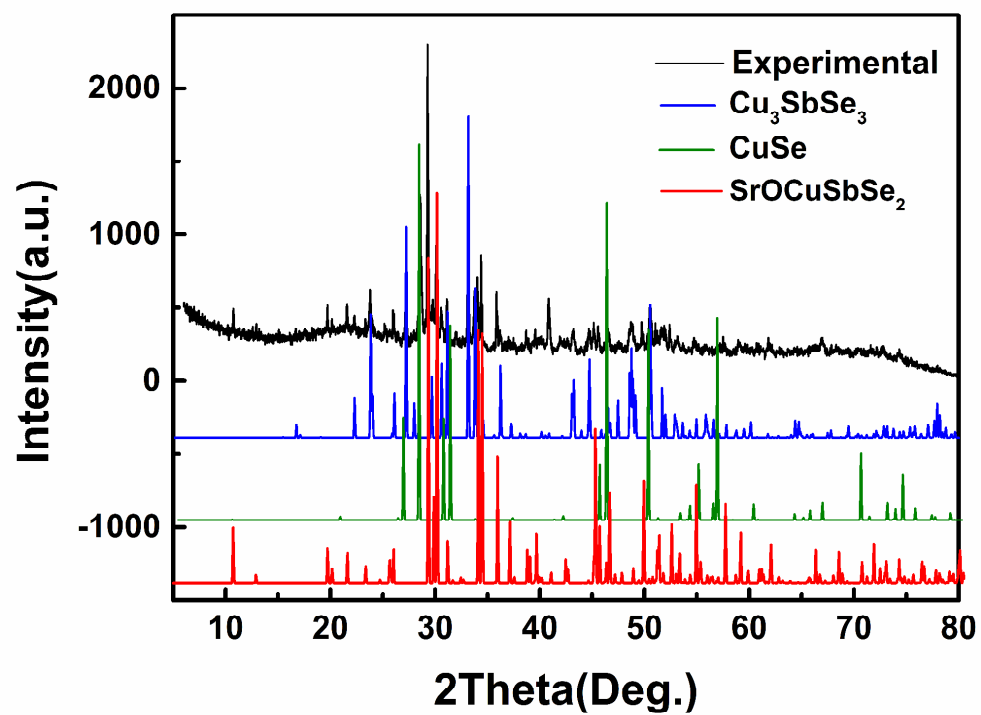


Figure S6. Powder X-ray diffraction patterns of the samples obtained after TG and DTA measurements of SrOCuSbSe_2 .

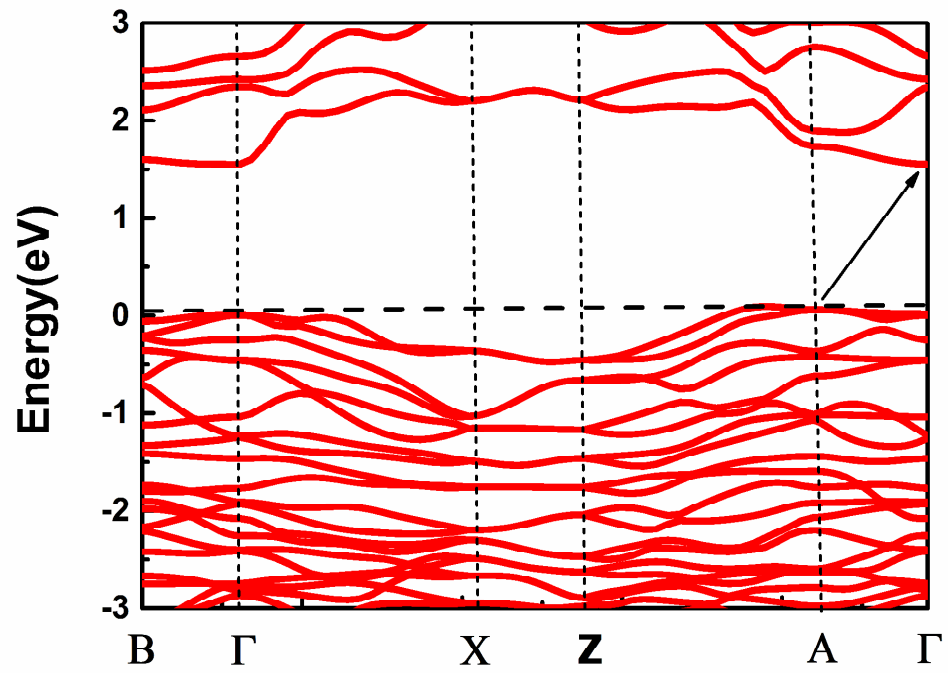


Figure S7. Band structure of SrOCuSbSe₂.

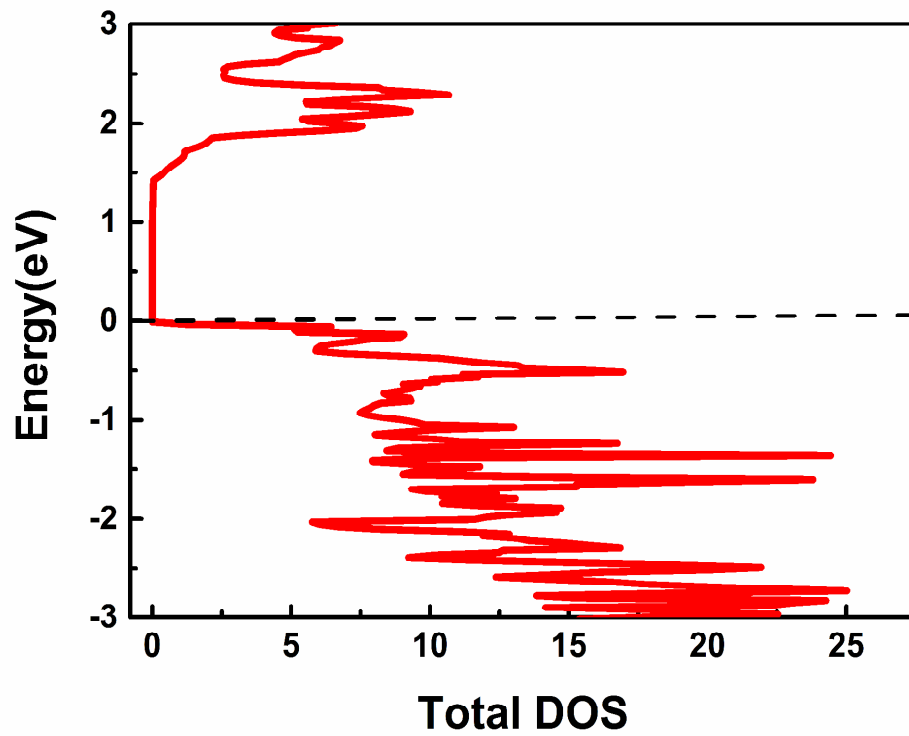


Figure S8. Total DOS of SrOCuSbSe₂.

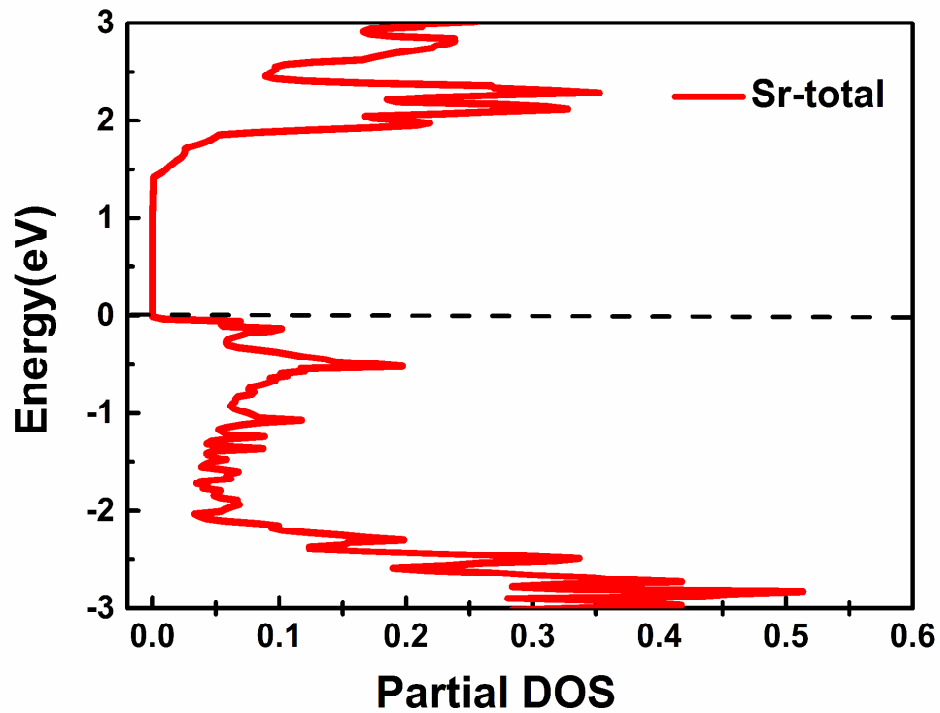


Figure S9. The total density of states of Sr^{2+} ions in SrOCuSbSe_2 .

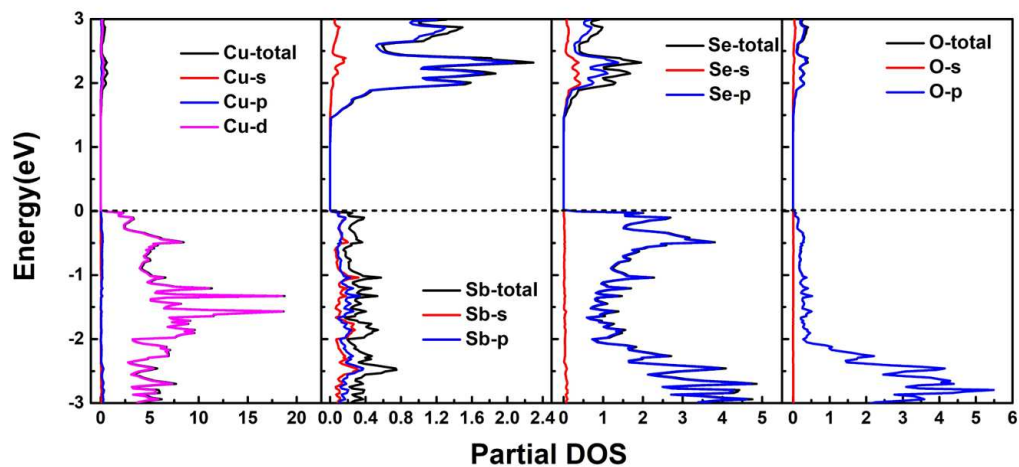


Figure S10. Partial DOS of each component in the compound.

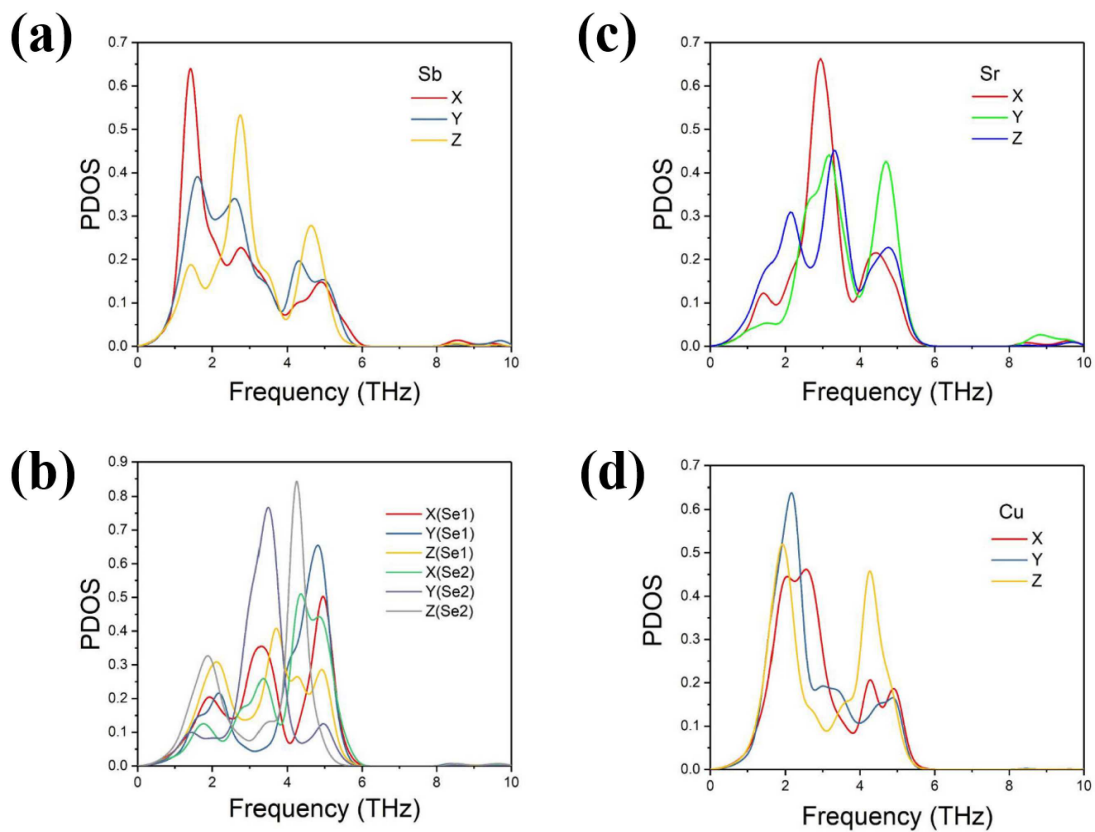


Figure S11. Partial DOS for (a) Sb, (b) Sr, (c) Se and (d) Cu atoms in different orientations.

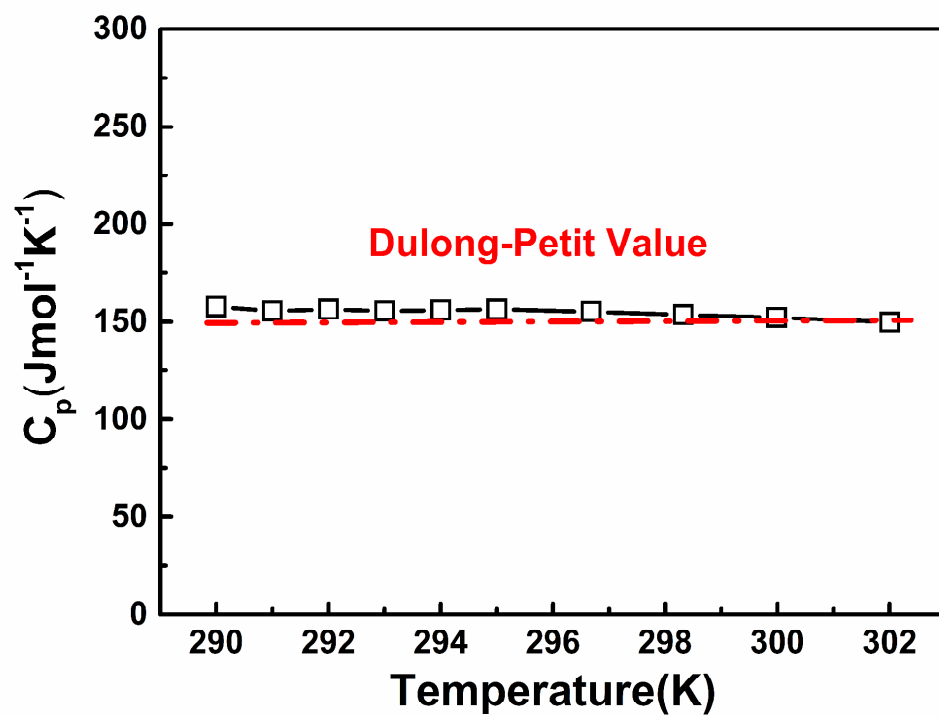


Figure S12. The curve of $C_p \sim$ Temperature (RT).

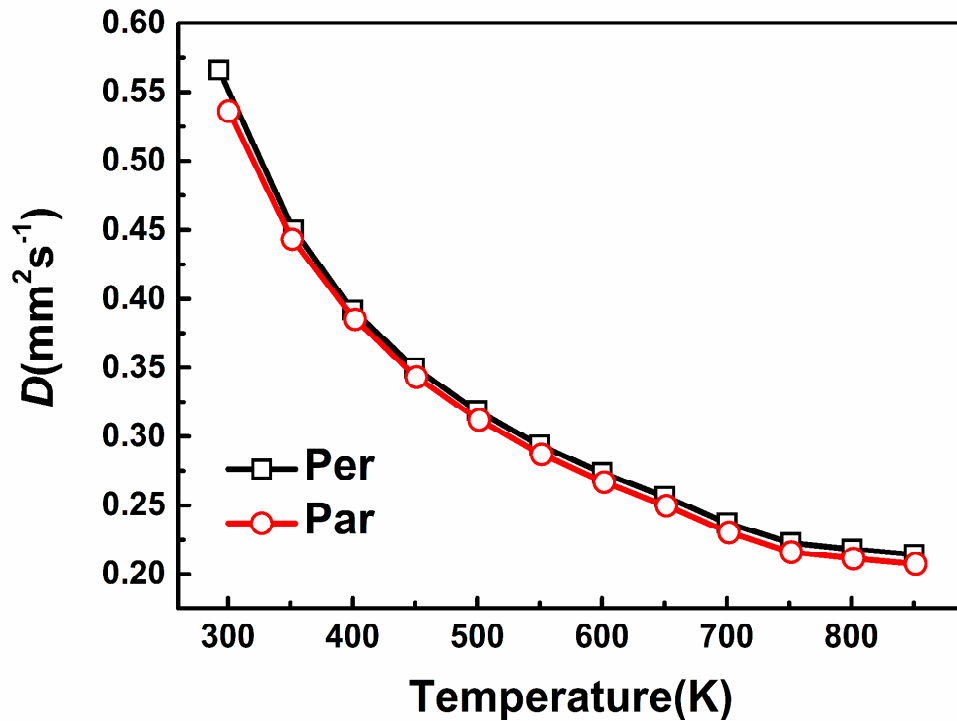


Figure S13. Thermal diffusivities of the SPSed polycrystalline SrOCuSbSe₂ (Per: the perpendicular direction of SPS pressure, Par: the parallel direction of SPS pressure).

7. Supplementary tables

Table S1. EDS results of SrOCuSbSe₂.

Element	Weight%	Atomic%
O K	2.73	13.22
Se K	33.52	32.90
Cu K	13.25	16.16
Sr L	22.49	19.89
Sb L	28.00	17.82
Totals	100.00	100.00

Table S2. Elastic properties of SrOCuSbSe₂ at room temperature.

Parameters		
Longitudinal sound velocity	v_l (m s ⁻¹)	3458.0
Transverse sound velocity	v_s (m s ⁻¹)	1900.2
Average sound velocity	v_a (m s ⁻¹)	2603.9

Table S3. High-temperature thermoelectric properties of SrOCuSbSe₂ compared to some well-known thermoelectric materials.

Material	T(K)	σ (S m ⁻¹)	S (μ V K ⁻¹)	k (W m ⁻¹ K ⁻¹)	ZT
BiCuSeO ²⁴	923	1120	410	0.40	0.43
SrOCuSbSe₂	850	366	522	0.38	0.22
SnSe ²⁵	750	612	450	0.30	0.31
AgSbSe ₂ ¹⁹	705	900	461	0.41	0.33
Cu ₂ CdSnSe ₄ ²⁶	700	3131	298	1.01	0.19
PbTe ²⁷	690	50000	-144	1.95	0.37
Cu ₁₂ Sb ₄ S ₁₃ ²⁸	673	117649	103	1.5	0.56
CuSbSe ₂ ²⁹	625	488	535	0.38	0.25
Cu ₂₂ Fe ₈ Ge ₄ S ₃₂ ³⁰	575	18877	133	1.2	0.16
Cu ₃ SbSe ₃ ³¹	550	393	190	0.26	0.03
Cu ₃ SbSe ₄ ³¹	523	4545	350	1.5	0.29

Table S4. Crystal Data and details of the structure refinements for SrOCuSbSe₂.

Chemical formula	SrOCuSbSe ₂
------------------	------------------------

F_w (g·mol ⁻¹)	446.83
Crystal system	Monoclinic
Space group	C_{2h}^2 - $P2_1/m$ (No. 11)
a (Å)	7.641(2)
b (Å)	4.0199(11)
c (Å)	9.013(3)
β (deg)	113.764(9)
V (Å ³)	253.37(13)
Z	2
Crystal color	Black
ρ_c (g·cm ⁻³)	5.857
μ (mm ⁻¹)	34.14
$F(000)$	388
R_{int}	0.151
R_1 [$I > 2\sigma(I)$]	0.039
wR_2 (all data)	0.067
GOF	0.99

^a $R_1 = \sum ||F_o| - |F_c|| / \sum |F_o|$. ^b $wR_2 = \{ \sum [w(F_o^2 - F_c^2)^2] / \sum [w(F_o^2)^2] \}^{1/2}$, $w = 1 / [\sigma^2(F_o^2) + (0.1000P)^2]$, where $P = (F_o^2 + 2F_c^2) / 3$.

Table S5. Atomic coordinates and isotropic displacement parameters (Å²) of the SrOCuSbSe₂ compound refined from single X-ray diffraction data recorded at room temperature.

atom	site	occ	x	y	z	$U_{\text{iso}}^*/U_{\text{eq}}$
Sb	2e	1	0.3836 (1)	0.75	0.2976 (1)	0.0128 (3)

Sr	2e	1	0.1529 (2)	0.25	-0.0904 (2)	0.0101 (4)
O	2e	1	0.178 (1)	0.75	0.083 (1)	0.0123 (8)
Cu	2e	1	0.8621 (3)	0.25	0.4641 (3)	0.0205 (6)
Se1	2e	1	0.8729 (2)	-0.25	0.6349 (2)	0.0104 (4)
Se2	2e	1	0.5725 (2)	0.25	0.2074 (2)	0.0115 (4)

Table S6. Atomic displacement parameters (\AA^2) of SrOCuSbSe₂.

	U_{11}	U_{22}	U_{33}	U_{12}	U_{13}	U_{23}
Sb	0.0113 (6)	0.0129 (6)	0.0082 (7)	0	-0.0023 (5)	0
Sr	0.0107 (8)	0.0091 (9)	0.0088 (10)	0	0.0022 (7)	0
Se1	0.0101 (8)	0.0105 (9)	0.0093 (10)	0	0.0025 (7)	0
Se2	0.0078 (9)	0.0124 (10)	0.0123 (10)	0	0.0021 (8)	0
Cu	0.0199 (12)	0.0225 (13)	0.0176 (14)	0	0.0061 (10)	0
O	0.0107 (12)	0.0128 (12)	0.0080 (11)	0	-0.0020 (10)	0

Table S7. Bond distances (\AA) and bond angles ($^\circ$) of SrOCuSbSe₂.

	Bond distances (\AA)		Bond distances (\AA)
Sb—O	1.942 (9)	Sr—Se1 ^{vii}	3.2367 (18)
Sb—Se2 ⁱ	2.7803 (15)	Sr—Se2	3.248 (2)
Sb—Se2	2.7804 (15)	Sr—Se2 ^{viii}	3.3674 (18)
Sb—Se1 ⁱⁱ	3.0353 (15)	Sr—Se2 ^{ix}	3.3674 (18)
Sb—Se1 ⁱⁱⁱ	3.0353 (15)	Sr—Cu ^{vi}	3.724 (3)
Sb—Sr ^{iv}	3.758 (2)	Se1—Cu ^v	2.5125 (16)

Sb—Sr	3.7957 (18)	Se1—Cu	2.5125 (16)
Sb—Sr ⁱ	3.7957 (18)	Se1—Cu ^x	2.521 (3)
Sr—O	2.503 (6)	Se2—Cu	2.475 (3)
Sr—O ^v	2.503 (6)	Cu—Cu ^{xi}	2.793 (3)
Sr—O ^{iv}	2.556 (10)	Cu—Cu ^x	2.793 (3)
Sr—Se1 ^{vi}	3.2367 (18)		
Bond angles (°)		Bond angles (°)	
O—Sb—Se2 ⁱ	90.9 (2)	Se1 ^{vi} —Sr—Sb	162.16 (6)
O—Sb—Se2	90.9 (2)	Se1 ^{vii} —Sr—Sb	107.11 (3)
Se2 ⁱ —Sb—Se2	92.59 (6)	Se2—Sr—Sb	45.68 (3)
O—Sb—Se1 ⁱⁱ	82.6 (2)	Se2 ^{viii} —Sr—Sb	81.70 (4)
Se2 ⁱ —Sb—Se1 ⁱⁱ	172.14 (5)	Se2 ^{ix} —Sr—Sb	119.20 (5)
Se2—Sb—Se1 ⁱⁱ	91.90 (4)	Cu ^{vi} —Sr—Sb	147.898 (18)
O—Sb—Se1 ⁱⁱⁱ	82.6 (2)	Sb ^{iv} —Sr—Sb	117.80 (4)
Se2 ⁱ —Sb—Se1 ⁱⁱⁱ	91.90 (4)	Sb ^v —Sr—Sb	63.95 (4)
Se2—Sb—Se1 ⁱⁱⁱ	172.14 (5)	Cu ^v —Se1—Cu	106.26 (10)
Se1 ⁱⁱ —Sb—Se1 ⁱⁱⁱ	82.94 (5)	Cu ^v —Se1—Cu ^x	67.42 (6)
O—Sb—Sr ^{iv}	38.9 (3)	Cu—Se1—Cu ^x	67.42 (6)
Se2 ⁱ —Sb—Sr ^{iv}	116.46 (4)	Cu ^v —Se1—Sb ⁱⁱ	74.24 (5)
Se2—Sb—Sr ^{iv}	116.46 (4)	Cu—Se1—Sb ⁱⁱ	142.00 (8)
Se1 ⁱⁱ —Sb—Sr ^{iv}	55.70 (4)	Cu ^x —Se1—Sb ⁱⁱ	138.31 (3)
Se1 ⁱⁱⁱ —Sb—Sr ^{iv}	55.70 (4)	Cu ^v —Se1—Sb ⁱⁱⁱ	142.00 (8)
O—Sb—Sr	36.11 (13)	Cu—Se1—Sb ⁱⁱⁱ	74.25 (5)
Se2 ⁱ —Sb—Sr	102.50 (5)	Cu ^x —Se1—Sb ⁱⁱⁱ	138.31 (3)
Se2—Sb—Sr	56.69 (4)	Sb ⁱⁱ —Se1—Sb ⁱⁱⁱ	82.94 (5)

Se1 ⁱⁱ —Sb—Sr	74.72 (4)	Cu ^v —Se1—Sr ^{xii}	144.47 (7)
Se1 ⁱⁱⁱ —Sb—Sr	115.96 (5)	Cu—Se1—Sr ^{xii}	79.65 (5)
Sr ^{iv} —Sb—Sr	62.20 (4)	Cu ^x —Se1—Sr ^{xii}	83.87 (6)
O—Sb—Sr ⁱ	36.11 (13)	Sb ⁱⁱ —Se1—Sr ^{xii}	122.61 (7)
Se2 ⁱ —Sb—Sr ⁱ	56.69 (4)	Sb ⁱⁱⁱ —Se1—Sr ^{xii}	73.53 (4)
Se2—Sb—Sr ⁱ	102.50 (5)	Cu ^v —Se1—Sr ^{xiii}	79.65 (5)
Se1 ⁱⁱ —Sb—Sr ⁱ	115.96 (5)	Cu—Se1—Sr ^{xiii}	144.47 (7)
Se1 ⁱⁱⁱ —Sb—Sr ⁱ	74.72 (4)	Cu ^x —Se1—Sr ^{xiii}	83.87 (6)
Sr ^{iv} —Sb—Sr ⁱ	62.20 (4)	Sb ⁱⁱ —Se1—Sr ^{xiii}	73.53 (4)
Sr—Sb—Sr ⁱ	63.95 (4)	Sb ⁱⁱⁱ —Se1—Sr ^{xiii}	122.61 (7)
O—Sr—O ^v	106.8 (4)	Sr ^{xii} —Se1—Sr ^{xiii}	76.78 (5)
O—Sr—O ^{iv}	79.1 (3)	Cu—Se2—Sb	95.77 (6)
O ^v —Sr—O ^{iv}	79.1 (3)	Cu—Se2—Sb ^v	95.77 (6)
O—Sr—Se1 ^{vi}	146.7 (2)	Sb—Se2—Sb ^v	92.59 (6)
O ^v —Sr—Se1 ^{vi}	80.72 (19)	Cu—Se2—Sr	170.30 (9)
O ^{iv} —Sr—Se1 ^{vi}	70.44 (17)	Sb—Se2—Sr	77.62 (5)
O—Sr—Se1 ^{vii}	80.72 (19)	Sb ^v —Se2—Sr	77.62 (5)
O ^v —Sr—Se1 ^{vii}	146.7 (2)	Cu—Se2—Sr ^{viii}	81.80 (6)
O ^{iv} —Sr—Se1 ^{vii}	70.44 (17)	Sb—Se2—Sr ^{viii}	97.04 (3)
Se1 ^{vi} —Sr—Se1 ^{vii}	76.78 (5)	Sb ^v —Se2—Sr ^{viii}	170.25 (5)
O—Sr—Se2	71.5 (2)	Sr—Se2—Sr ^{viii}	105.88 (6)
O ^v —Sr—Se2	71.5 (2)	Cu—Se2—Sr ^{ix}	81.80 (6)
O ^{iv} —Sr—Se2	129.4 (2)	Sb—Se2—Sr ^{ix}	170.25 (5)
Se1 ^{vi} —Sr—Se2	139.48 (3)	Sb ^v —Se2—Sr ^{ix}	97.04 (3)
Se1 ^{vii} —Sr—Se2	139.48 (3)	Sr—Se2—Sr ^{ix}	105.88 (6)

O—Sr—Se2 ^{viii}	79.3 (2)	Sr ^{viii} —Se2—Sr ^{ix}	73.30 (5)
O ^v —Sr—Se2 ^{viii}	140.7 (2)	Se2—Cu—Se1 ⁱ	111.66 (7)
O ^{iv} —Sr—Se2 ^{viii}	139.15 (10)	Se2—Cu—Se1	111.66 (7)
Se1 ^{vi} —Sr—Se2 ^{viii}	115.75 (6)	Se1 ⁱ —Cu—Se1	106.26 (10)
Se1 ^{vii} —Sr—Se2 ^{viii}	72.13 (5)	Se2—Cu—Se1 ^x	102.25 (10)
Se2—Sr—Se2 ^{viii}	74.12 (6)	Se1 ⁱ —Cu—Se1 ^x	112.58 (6)
O—Sr—Se2 ^{ix}	140.7 (2)	Se1—Cu—Se1 ^x	112.58 (6)
O ^v —Sr—Se2 ^{ix}	79.3 (2)	Se2—Cu—Cu ^{xi}	121.56 (9)
O ^{iv} —Sr—Se2 ^{ix}	139.15 (10)	Se1 ⁱ —Cu—Cu ^{xi}	56.43 (6)
Se1 ^{vi} —Sr—Se2 ^{ix}	72.13 (5)	Se1—Cu—Cu ^{xi}	126.75 (12)
Se1 ^{vii} —Sr—Se2 ^{ix}	115.75 (6)	Se1 ^x —Cu—Cu ^{xi}	56.15 (7)
Se2—Sr—Se2 ^{ix}	74.12 (6)	Se2—Cu—Cu ^x	121.56 (9)
Se2 ^{viii} —Sr—Se2 ^{ix}	73.30 (5)	Se1 ⁱ —Cu—Cu ^x	126.75 (12)
O—Sr—Cu ^{vi}	122.27 (19)	Se1—Cu—Cu ^x	56.43 (6)
O ^v —Sr—Cu ^{vi}	122.27 (19)	Se1 ^x —Cu—Cu ^x	56.15 (7)
O ^{iv} —Sr—Cu ^{vi}	82.1 (2)	Cu ^{xi} —Cu—Cu ^x	92.04 (12)
Se1 ^{vi} —Sr—Cu ^{vi}	41.59 (3)	Se2—Cu—Sr ^{xii}	158.18 (9)
Se1 ^{vii} —Sr—Cu ^{vi}	41.59 (3)	Se1 ⁱ —Cu—Sr ^{xii}	58.77 (5)
Se2—Sr—Cu ^{vi}	148.48 (7)	Se1—Cu—Sr ^{xii}	58.77 (5)
Se2 ^{viii} —Sr—Cu ^{vi}	80.73 (5)	Se1 ^x —Cu—Sr ^{xii}	99.57 (8)
Se2 ^{ix} —Sr—Cu ^{vi}	80.73 (5)	Cu ^{xi} —Cu—Sr ^{xii}	71.56 (8)
O—Sr—Sb ^{iv}	95.9 (2)	Cu ^x —Cu—Sr ^{xii}	71.56 (8)
O ^v —Sr—Sb ^{iv}	95.9 (2)	Se2—Cu—Sr ^{ix}	59.10 (6)
O ^{iv} —Sr—Sb ^{iv}	28.5 (2)	Se1 ⁱ —Cu—Sr ^{ix}	158.02 (6)
Se1 ^{vi} —Sr—Sb ^{iv}	50.77 (3)	Se1—Cu—Sr ^{ix}	95.70 (4)

Se1 ^{vii} —Sr—Sb ^{iv}	50.77 (3)	Se1 ^x —Cu—Sr ^{ix}	55.95 (5)
Se2—Sr—Sb ^{iv}	157.91 (6)	Cu ^{xi} —Cu—Sr ^{ix}	109.20 (10)
Se2 ^{viii} —Sr—Sb ^{iv}	122.49 (5)	Cu ^x —Cu—Sr ^{ix}	65.43 (7)
Se2 ^{ix} —Sr—Sb ^{iv}	122.49 (5)	Sr ^{xiii} —Cu—Sr ^{ix}	136.99 (4)
Cu ^{vi} —Sr—Sb ^{iv}	53.61 (4)	Se2—Cu—Sr ^{viii}	59.10 (6)
O—Sr—Sb ^v	87.76 (19)	Se1 ⁱ —Cu—Sr ^{viii}	95.70 (4)
O ^v —Sr—Sb ^v	27.21 (19)	Se1—Cu—Sr ^{viii}	158.02 (6)
O ^{iv} —Sr—Sb ^v	94.11 (19)	Se1 ^x —Cu—Sr ^{viii}	55.95 (5)
Se1 ^{vi} —Sr—Sb ^v	107.11 (3)	Cu ^{xi} —Cu—Sr ^{viii}	65.43 (7)
Se1 ^{vii} —Sr—Sb ^v	162.16 (6)	Cu ^x —Cu—Sr ^{viii}	109.20 (10)
Se2—Sr—Sb ^v	45.68 (3)	Sr ^{xiii} —Cu—Sr ^{viii}	136.99 (4)
Se2 ^{viii} —Sr—Sb ^v	119.20 (5)	Sr ^{ix} —Cu—Sr ^{viii}	62.32 (5)
Se2 ^{ix} —Sr—Sb ^v	81.70 (4)	Sb—O—Sr	116.7 (3)
Cu ^{vi} —Sr—Sb ^v	147.897 (19)	Sb—O—Sr ⁱ	116.7 (3)
Sb ^{iv} —Sr—Sb ^v	117.80 (4)	Sr—O—Sr ⁱ	106.8 (4)
O—Sr—Sb	27.21 (19)	Sb—O—Sr ^{iv}	112.6 (4)
O ^v —Sr—Sb	87.76 (19)	Sr—O—Sr ^{iv}	100.9 (3)
O ^{iv} —Sr—Sb	94.11 (19)	Sr ⁱ —O—Sr ^{iv}	100.9 (3)

Symmetry codes: (i) x, y+1, z; (ii) -x+1, -y, -z+1; (iii) -x+1, -y+1, -z+1; (iv) -x, -y+1, -z; (v) x, y-1, z; (vi) x-1, y, z-1; (vii) x-1, y+1, z-1; (viii) -x+1, -y+1, -z; (ix) -x+1, -y, -z; (x) -x+2, -y, -z+1; (xi) -x+2, -y+1, -z+1; (xii) x+1, y, z+1; (xiii) x+1, y-1, z+1.

Table S8. Debye temperatures (θ), group velocities (v), and Grüneisen parameters (γ) for the SrOCuSbSe₂ compounds.

	TA	TA'	LA
$\theta(K)$	71	74	90
$v(m/s)$	1975	2145	4276
γ	3.244	3.235	2.495

REFERENCES

- (1) Sheldrick, G. Crystal structure refinement with SHELXL. *Acta Crystallogr., Sect C* **2015**, *71*, 3-8.
- (2) Kortüm, G.; Braun, W.; Herzog, G. Principles and Techniques of Diffuse-Reflectance Spectroscopy. *Angew. Chem. Int. Ed.* **1963**, *2*, 333-341.
- (3) Kresse, G.; Hafner, J. Ab initio molecular dynamics for liquid metals. *Phys. Rev. B* **1993**, *47*, 558-559.
- (4) Kresse, G.; Furthmüller, J. Efficiency of ab-initio total energy calculations for metals and semiconductors using a plane-wave basis set. *Comput. Mater. Sci.* **1996**, *6*, 15-50.
- (5) Kresse, G.; Furthmüller, J. Efficient iterative schemes for ab initio total-energy calculations using a plane-wave basis set. *Phys. Rev. B* **1996**, *54*, 11169-11186.
- (6) Perdew, J. P.; Burke, K.; Ernzerhof, M. Generalized gradient approximation made simple. *Phys. Rev. Lett.* **1996**, *77*, 3865-3868.
- (7) Parliński, K. Software Phonon, Cracow (2001) as implemented in MedeA 2.2. *Materials Design, Angel Fire, New Mexico.* **2005**.

- (8) Parlinski, K.; Li, Z.; Kawazoe, Y. First-principles determination of the soft mode in cubic ZrO_2 . *Phys. Rev. Lett.* **1997**, *78*, 4063-4066.
- (9) Zhou, J.; Bian, G. Q.; Zhu, Q. Y.; Zhang, Y.; Li, C. Y.; Dai, J. Solvothermal crystal growth of CuSbQ_2 (Q= S, Se) and the correlation between macroscopic morphology and microscopic structure. *J. Solid State Chem.* **2009**, *182*, 259-264.
- (10) Liu, C.; Hou, P.; Chai, W.; Tian, J.; Zheng, X.; Shen, Y.; Zhi, M.; Zhou, C.; Liu, Y. Hydrazine-hydrothermal syntheses, characterizations and photoelectrochemical properties of two quaternary chalcogenidoantimonates (III) BaCuSbQ_3 (Q= S, Se). *J. Alloys Compd.* **2016**, *679*, 420-425.
- (11) Pfitzner, A. Cu_3SbSe_3 : Synthese und Kristallstruktur. *Z. Anorg. Allg. Chem.* **1995**, *621*, 685-688.
- (12) Liu, C.; Shen, Y.; Hou, P.; Zhi, M.; Zhou, C.; Chai, W.; Cheng, J. W.; Liu, Y. Hydrazine-Hydrothermal Synthesis and Characterization of the Two New Quaternary Thioantimonates (III) BaAgSbS_3 and $\text{BaAgSbS}_3 \cdot \text{H}_2\text{O}$. *Inorg. Chem.* **2015**, *54*, 8931-8936.
- (13) Pfitzner, A. Crystal structure of tricopper tetraselenoantimonate (V), Q_3SbSe_4 . *Z. Kristallogr. Cryst. Mater.* **1994**, *209*, 685-685.
- (14) Skoug, E. J.; Morelli, D. T. Role of lone-pair electrons in producing minimum thermal conductivity in nitrogen-group chalcogenide compounds. *Phys. Rev. Lett.* **2011**, *107*, 235901, 1-5.
- (15) Tan, G.; Zhao, L. D.; Kanatzidis, M. G. Rationally designing high-performance bulk thermoelectric materials. *Chem. Rev.* **2016**, *116*, 12123-12149.
- (16) Mott, N. Conduction in glasses containing transition metal ions. *J. Non-Crys Solids* **1968**, *1*, 1-17.

- (17) Mott, N. F.; Davis, E. A. Electronic processes in non-crystalline materials. *OUP Oxford*: **2012**.
- (18) Wojciechowski, K.; Schmidt, M. Structural and thermoelectric properties of AgSbTe₂-AgSbSe₂ pseudobinary system. *Phys. Rev. B* **2009**, *79*, 184202, 1-7.
- (19) Guin, S. N.; Chatterjee, A.; Negi, D. S.; Datta, R.; Biswas, K. High thermoelectric performance in tellurium free *p*-type AgSbSe₂. *Energy Environ. Sci.* **2013**, *6*, 2603-2608.
- (20) Takahashi, H.; Raghavendra, N.; Gascoin, F.; Pelloquin, D.; Hébert, S.; Guilmeau, E. Transport Properties of an Intermetallic with Pseudo-hollandite Structure as a Potential Thermoelectric Material: The Example of Tl_xCr₅Se₈. *Chem. Mater.* **2013**, *25*, 1809-1815.
- (21) Morelli, D.; Jovovic, V.; Heremans, J. Intrinsically minimal thermal conductivity in cubic I–V–VI₂ Semiconductors. *Phys. Rev. Lett* **2008**, *101*, 035901, 1-4.
- (22) Pei, Y. L.; He, J.; Li, J. F.; Li, F.; Liu, Q.; Pan, W.; Barreteau, C.; Berardan, D.; Dragoe, N.; Zhao, L. D. High thermoelectric performance of oxyselenides: intrinsically low thermal conductivity of Ca-doped BiCuSeO. *NPG Asia Mater.* **2013**, *5*, e47, 1-9.
- (23) Kurosaki, K.; Kosuga, A.; Muta, H.; Uno, M.; Yamanaka, S. Ag₉TlTe₅: A high-performance thermoelectric bulk material with extremely low thermal conductivity. *Appl. Phys. Lett.* **2005**, *87*, 061919, 1-3.
- (24) Zhao, L. D.; He, J.; Berardan, D.; Lin, Y.; Li, J. F.; Nan, C. W.; Dragoe, N. BiCuSeO oxyselenides: new promising thermoelectric materials. *Energy Environ. Sci.* **2014**, *7*, 2900-2924.
- (25) Chen, C. L.; Wang, H.; Chen, Y. Y.; Day, T.; Snyder, G. J. Thermoelectric properties of *p*-type polycrystalline SnSe doped with Ag. *J. Mater. Chem. A* **2014**, *2*, 11171-11176.

- (26) Liu, M. L.; Chen, I. W.; Huang, F. Q.; Chen, L. D. Improved Thermoelectric Properties of Cu-Doped Quaternary Chalcogenides of $\text{Cu}_2\text{CdSnSe}_4$. *Adv. Mater.* **2009**, *21*, 3808-3812.
- (27) Pei, Y. L.; Liu, Y. Electrical and thermal transport properties of Pb-based chalcogenides: PbTe, PbSe, and PbS. *J. Alloys Compd.* **2012**, *514*, 40-44.
- (28) Lai, W.; Wang, Y.; Morelli, D. T.; Lu, X. From bonding asymmetry to anharmonic rattling in $\text{Cu}_{12}\text{Sb}_4\text{S}_{13}$ tetrahedrites: When lone-pair electrons are not so lonely. *Adv. Funct. Mater.* **2015**, *25*, 3648-3657.
- (29) Zhang, D.; Yang, J.; Jiang, Q.; Fu, L.; Xiao, Y.; Luo, Y.; Zhou, Z. Ternary CuSbSe_2 chalcostibite: facile synthesis, electronic-structure and thermoelectric performance enhancement. *J. Mater. Chem. A* **2016**, *4*, 4188-4193.
- (30) Pavan Kumar, V.; Paradis-Fortin, L.; Lemoine, P.; Caignaert, V.; Raveau, B.; Malaman, B.; Le Caër, G. r.; Cordier, S. p.; Guilmeau, E. Designing a Thermoelectric Copper-Rich Sulfide from a Natural Mineral: Synthetic Germanite $\text{Cu}_{22}\text{Fe}_8\text{Ge}_4\text{S}_{32}$. *Inorg. Chem.* **2017**, *56*, 13376-13381.
- (31) Tyagi, K.; Gahtori, B.; Bathula, S.; Toutam, V.; Sharma, S.; Singh, N. K.; Dhar, A. Thermoelectric and mechanical properties of spark plasma sintered Cu_3SbSe_3 and Cu_3SbSe_4 : Promising thermoelectric materials. *Appl. Phys. Lett.* **2014**, *105*, 261902, 1-5.